CHALMERS
UNIVERSITY OF TECHNOLOGY

Optical properties of marine aerosol: modelling the transition from dry, irregularly shaped crystals to brine-coated, dissolving salt particles

Journal of Quantitative Spectroscopy & Radiative Transfer 295 (2022) 108408

Contents lists available at ScienceDirect

Journal of Quantitative Spectroscopy & Radiative Transfer

journal homepage: www.elsevier.com/locate/jqsrt

Optical properties of marine aerosol: modelling the transition from dry, irregularly shaped crystals to brine-coated, dissolving salt particles

Michael Kahnert[a,b,*], Franz Kanngießer[c]

[a] Research Department, Swedish Meteorological and Hydrological Institute, Folkborgsvägen 17, Norrköping SE-601 76, Sweden
[b] Department of Space, Earth and Environment, Chalmers University of Technology, Maskingränd 2, Gothenburg SE-412 96, Sweden
[c] Institute of Geophysics and Meteorology, University of Cologne, Cologne DE-50969, Germany

ARTICLE INFO

Article history:
Received 21 June 2022
Revised 26 October 2022
Accepted 30 October 2022
Available online 04 November 2022

MSC:
0000
1111

PACS:
0000
1111

Keywords:
marine aerosol
lidar
remote sensing
aerosol optics

ABSTRACT

An aerosol-optics model for water-coated marine aerosols is introduced that accounts for irregularities in the geometry of dry salt particles, and that mimics the processes of water-adsorption, dissolution of salt, and rearrangement of the liquid mantle following dissolution. The model can be tuned to adjust how rapidly the dry salt particles become spherical as water is being added to them. Size-shape distributions of the model are generated and employed to compute the ensemble-averaged extinction and backscattering cross sections, the lidar ratio, and the linear backscatter depolarisation ratio (LDR). A power law distribution that is frequently used in chemical transport models yields lidar ratios and LDR values that are consistent with field and satellite observations. But the results are found to be quite sensitive to the assumed size distribution. A generic lognormal size distribution tends to produce higher extinction cross sections, backscattering cross sections, and somewhat higher lidar ratios than the power-law distribution, while the depolarisation ratios are of comparable magnitude. We further gauged the model's performance by comparing it with homogeneous superellipsoids. For a salt mass fraction of 0.97, the cross sections and the lidar ratio of cubic superellipsoids (i.e., those with unit aspect ratios) agree best with the reference model over all effective radii at a superellipsoid roundness parameter of 0.6. The LDR is more challenging to reproduce. For a salt mass fraction of 0.97, cubic homogeneous superellipsoids mostly give lower LDR values than the reference model. However, by increasing one aspect ratio, the superellipsoids can be tuned to yield higher LDR values. For a salt mass fraction of 0.91, the reference model yields LDR values below 0.1. Homogeneous superellipsoids that match the cross sections and lidar ratio of the reference model tend to give LDR values exceeding the reference results, at least for super-micron particles.

1. Introduction

Marine aerosols are the most abundant aerosol type in the atmosphere. Through their ability to act as cloud condensation nuclei they can impact cloud optical properties, cloud lifetime, and precipitation [1], thus influencing the radiative energy budget and the hydrological cycle. Representing these aerosol effects on the radiative balance in climate models can be challenging. For instance, inaccuracies in the description of marine aerosol effects in climate models can manifests themselves as model biases in sea-surface temperature, which has been reported to be particularly pronounced over the Southern Ocean [2,3]. In chemical transport models (CTMs), an accurate description of marine aerosol emission, transport, and deposition is important for several reasons. To study the health impact of particulate matter, it is imperative to correctly model how the total mass concentration is partitioned between natural particles, such as sea salt, and potentially harmful anthropogenic components, such as soot or sulphate. Also, sea-salt deposition over land impacts soil chemistry by counteracting the effect of acidifying pollutants, which is important to ecosystem modelling. However, recent model evaluations (e.g. [4]) revealed that some of the state-of-the art CTMs tend to underestimate in situ observations of near-surface concentrations as well as wet deposition of marine aerosols.

Evaluation of highly complex, large-scale environmental modelling systems, such as CTMs and climate models, is a formidable task. The most important source of error in CTMs tends to be the

* Corresponding author.
E-mail address: michael.kahnert@smhi.se (M. Kahnert).

https://doi.org/10.1016/j.jqsrt.2022.108408

emission flux. One common approach of evaluating models is to compare observations with model output (e.g. mass concentrations of long-range transported particles). This is far from straight forward, because the model output can be compromised by a number of different error sources other than the emission flux. Arguably a more robust approach is to make use of measurements that are very close to the source regions, because they are likely to provide a good proxy for the emissions themselves. For marine aerosols, the main problem is that in situ measurements over the remote oceans are very sparse in time and space. However, long time series of data with good spatial coverage are essential for comprehensively evaluating global environmental modelling systems. Such data sets can be provided by satellites. One challenge in interpreting satellite observations of aerosols is to extract information on aerosol composition and physical properties, which is required for comparing the observations to model in- and output variables. The critical link between observations and CTMs or climate models is provided by aerosol-optics models (e.g. [5,6]).

Marine aerosols contain mostly sodium chloride, but also organic substances, potassium, magnesium, calcium, and dimethyl sulphide (e.g. [7]). Their number density is strongly dependent on wind speed, while their size can depend on sea-surface temperature and salinity (e.g. [8]). The water content is highly variable and depends mostly on ambient relative humidity (e.g. [7]). In order to monitor the concentration, mean size, and water content of marine aerosols by remote sensing techniques, we need to understand how aerosol morphology and composition are related to radiative and polarimetric properties.

Pristine sodium chloride crystals have cubic shape. Dry sea-salt particles in nature can also be cubical [9], but they can also deviate from cubic shape (e.g. [10]). Cubes are often employed as a canonical shape to model optical properties of sea-salt aerosols [9,11–15]. Departures from cubic shape have been considered in various modelling approaches comprising superellipsoids [16–18], Gaussian random cubes [19] and convex polyhedra [18,19]. Superellipsoids are a highly flexible and comprehensive class of model particles covering an enormous range of optical properties that exceeds that of typical marine aerosols [17]. Thus, this model needs to be properly constrained [18]. Convex polyhedra yield linear depolarisation ratio (LDR) values that are consistent with lidar field measurements [19], and they can be used to estimate uncertainties related to non-ideal cubic shapes.

Mixing sea-salt with water alters the dielectric and morphological, thus the optical properties. The addition of water generally increases the optical cross sections and quenches LDR. The details of this effect are poorly understood, as laboratory measurements are sparse [13]. Thus it is imperative to develop a versatile reference model, from which we can gain physical insight into the relation between morphology and optical properties. In [18] a model was proposed in which the morphology of wet marine aerosols is simulated by use of a pseudo-potential model. The purpose of our present study is two-fold.

1. The approach in [18] tends to coat the salt particles with a mantle that can deviate significantly from spherical shape, even for moderately thick coatings. Potentially, this can give rise to atypically high LDR values for particles with a thick water coating. Here we propose a significant modification of the model that rectifies this problem.
2. In [18] only three discrete particle sizes have been investigated. Here we perform computations for size-shape distributions of marine aerosols with a range of effective particle radii.

We will also make an attempt to gauge the prospects of using simplified particle models. To this end, we will consider homogeneous superellipsoids. For homogeneous particles with point-group symmetries, one can often significantly speed up light-scattering computations [20,21]. Fast optics models are often required in large-scale environmental applications, such as in chemical data assimilation (e.g. [22,23]).

In the following section we introduce the model particles, the model size distributions, and the numerical light-scattering methods relevant for this study. Results will be shown and discussed in Sections 3 and 4, respectively. Concluding remarks are given in Section 5.

2. Methods

2.1. Particle models

Dry marine aerosols. Dry, pristine sodium chloride crystals that form under ideal conditions have cubic shape. Sea-salt particles in nature that originate from emitted sea-spray contain mostly sodium chloride, but also potassium, calcium, magnesium, and organic substances. The shapes of these particles are more random, but often the cubic geometry still shows through in micrographs (e.g. [10,24–30]). For this reason, cubes have often been used as an idealised model geometry for marine aerosols [11–15,24]. However, randomised cubes are likely to be a more realistic model, although not any kind of randomisation model gives an equally good representation of the optical properties [19].

Presently the most promising candidate seems to be the convex polyhedra model introduced in [19]. In this approach one randomly places N_c points in a Cartesian coordinate system and applies a concave hull around these points [19,31]. Typically, for $N_c \ll 100$ one obtains random polyhedral shapes that show little similarity to that of a cube. For N_c on the order of 10^3 the convex polyhedra are very similar to ideal cubes. For N_c on the order of a few 100 one obtains distorted cubes that look similar to shapes of marine aerosols observed in micrographs.

We generated model particles with volume-equivalent radii r_V varying between 0.04 μm and 1.5 μm in size-steps of 0.02 μm. Thus we generate model particles with 74 discrete sizes. For each particle size, the number N_c of supporting points in the concave-hull construction was randomly selected between 100 and 300. Thus, the ensemble of particles we consider is both a size- and a random-shape distribution. The upper limit of our size-range is dictated by computational constraints in the numerical light-scattering computations with the discrete-dipole approximation (DDA), as explained below. The particles are discretised in a Cartesian grid, which is required as input to the DDA. The grid spacing d is chosen such that $|m|kd \lesssim 0.4$, where m is the complex refractive index of the scatterer, and $k = 2\pi/\lambda$ is the wavenumber based on the wavelength λ of the surrounding medium. It has been demonstrated in [19] that such a grid spacing is sufficiently fine to yield DDA results with an error variance that is significantly lower than that resulting from random variations in the particles' stochastic geometries, which is a lower bound for the uncertainties in our model.

Water-coated marine aerosols. Marine aerosols are emitted as sea-spray. Depending on ambient relative humidity, the water in the emitted droplets can partly or completely evaporate. Dry sea-salt particles are highly hygroscopic; in humid air water vapour can condense onto the particles, and the solid salt particle can partially or completely dissolve in the liquid coating. The microphysical cause of water condensation is the Coulomb interaction between salt ions and water-vapour molecules. This interaction is strongest for those ions on the particle surface that have a large number of neighbouring ions. On the other hand, those salt ions are most likely to be dissolved in a liquid coating that have the smallest number of neighbouring ions. In [18] a pseudo-potential model has been applied that mimics these effects. The pseudo-

potential is defined by

$$V_i = -\sum_{j=1}^{N} f_{ij}, \quad i = 1, \ldots, N_s \tag{1}$$

$$f_{ij} = \begin{cases} 1 & : \mid \mathbf{r}_i - \mathbf{r}_j \mid \leq R \\ 0 & : \text{otherwise} \end{cases}, \tag{2}$$

where N_s is the number of discrete cells on the particle surface that consist of either salt or liquid water. $\mathbf{r}_i$, $\mathbf{r}_j$ are the position vectors of cells i and j, where N is the total number of salt- or water-occupied cells in the discretised particle. R is a free tuning parameter that limits the radius within which neighbouring cells contribute to V_i. After computing V_i, the surface points are sorted by increasing potential. Subsets of equal potential are shuffled randomly.

The main problem is that the addition of water changes the surface of the particle, thus the surface potential. For this reason, the addition of material and the re-evaluation of the surface potential has to be done iteratively. This is done in a 2-step process, which closely follows the ideas of [32]. We denote this process by `add_coating`:

- Step 1. We set the radius of influence $R = 3d$, where d is the grid spacing. After computing the surface potential, we attach $N_{\text{add}} = \alpha_1 N_s$ water cells to the particle, starting with the surface points of lowest surface potential. We set $\alpha_1 = 0.04$.
- Step 2. We recompute the surface potential with a radius of influence $R = \max\{3d, R_{\text{cor}}\}$, where $R_{\text{cor}} = (d^2/r_{\text{V}})\sqrt{3N/(2\pi) - 1}$, where r_{V} is the volume-equivalent radius of the particle. Then we add another $N_{\text{add}} = \alpha_2 N_s$ liquid-water cells to the surface, starting with the surface points with the lowest potential. We set $\alpha_2 = 0.001$. Note that N and N_s are variables that change after each iteration step.

This 2-step process is an inner iteration in the construction of the model particles. However, we also need an outer iteration, which accounts for the fact that the solid salt core will gradually dissolve in the liquid water coating. For sea-salt we use the solubility of sodium chloride ϕ_b=36 g salt per 100 ml water (where the subscript b stands for brine). We also assume a brine density of 1210 kg/m^3, and a solid-phase salt density of 2240 kg/m^3. The resulting relations between the liquid-water volume and mass fractions, and the corresponding volume-equivalent particle radii are discussed in the appendix. The dissolution of salt in the liquid coating is modelled by a similar 2-step process, which we denote by `dissolve_salt`:

- Step 1. We set $R = 3d$ and dissolve $N_{\text{dis}} = \beta_1 N_s^{\text{coated}}$ solid salt cells, where N_s^{coated} is the number of grid cells at the surface of the solid salt core that are in immediate contact with liquid coating. The process starts by dissolving those salt cells with the *highest* surface potential. We set $\beta_1 = 0.0016$.
- Step 2. We recompute the surface potential with $R = \max\{3d, R_{\text{cor}}\}$ and dissolve $N_{\text{dis}} = \beta_2 N_s^{\text{coated}}$ solid salt cells, where $\beta_2 = 0.0004$.

Up to this point, our model follows the one described in [18]. However, we found that this model tends to require a lot of coating material before it approaches a spherical shape. For this reason, we added a third process that allows the liquid coating to rearrange itself after part of the solid salt has been dissolved and added to the liquid phase. We do assume that there is an immobile liquid surface layer of thickness d_0 which, owing to the Coulomb interaction, does not rearrange itself. The liquid outside this surface layer is regrouped toward a preferential spherical arrangement. We denote this process by `rearrange_coating`:

- In our testing of the model, we set $d_0 = 3d$. All liquid grid cells at a distance from the solid surface larger than $3d$ are flagged for rearrangement.
- All grid cells with coordinates (i, j, k) outside the surface layer are grouped into "onion shells", i.e., in ascending order of their distance to the origin $\sqrt{i^2 + j^2 + k^2}$. Groups of points with equal distance are randomly shuffled. The liquid grid cells flagged for rearrangement are distributed to those grid points in ascending order.

Here d_0 is a free parameter. Thus setting $d_0 = 3d$ only defines a particular instance of this class of model particles. By making other choices of d_0 one could tune the shape of partially-coated salt particles. Higher values d_0 will yield more non-spherical water coatings at intermediate stages of the coating process.

The complete construction algorithm of our model particles proceeds by iterating these three processes. When running the program one prescribes the volume-equivalent radius of the dry salt particle, the salt mass fraction f_m of the water-coated salt particle, the wavelength λ, and the complex refractive index m of salt and water at the specified wavelength. The size of the particle is converted to a number of grid cells N_{dry} occupied by the dry salt particle, using $|m|kd \lesssim 0.4$. From N_{dry} and f_m, the number of grid cells N_w is computed that needs to be occupied by water in order to reach this mass fraction. Thus the construction algorithm proceeds as follows:

```
DO WHILE N_w(now) < N_w
add_coating
dissolve_salt
rearrange_coating
END DO
```

where N_w(now) is that number of water grid-cells in the present iteration step.

For each of the 74 discrete particle sizes, we consider four sea-salt mass fractions, namely, f_m=1.00 (pure sea-salt), 0.97, 0.94, and 0.91. This braces the most interesting range of mass fractions, in which the transition from strong to weak depolarisation occurs. Figure 1 (top row) shows examples of the resulting model particles. The figure clearly illustrates that the addition of liquid water quickly rounds off the sharp edges of the salt core, which are the points with the highest surface potential. Also, the second top image from the left illustrates the thin liquid surface layer that remains stuck to the surface of the solid core. As more liquid water is applied, the coating approaches spherical shape, while the core becomes more and more rounded.

For dry sodium chloride at a wavelength of 532 nm, absorption is negligible. Thus the imaginary part of the complex refractive index m vanishes. We assume m_{NaCl}=1.5484 [33], and we use this value for dry sea-salt. The coating consists of a saturated salt solution (brine), for which we use the refractive index m_{brine}=1.334 + $6.19{\cdot}10^{-7}$i based on the parametrisation given in [34].

For comparison, we also performed computation for superellipsoids. The geometry of these particles is given in Cartesian coordinates by [35]

$$\left[\left(\frac{x}{a}\right)^{\frac{2}{e}} + \left(\frac{y}{b}\right)^{\frac{2}{e}}\right]^{\frac{e}{n}} + \left(\frac{z}{c}\right)^{\frac{2}{n}} = 1, \tag{3}$$

where a, b, and c denote the sizes of the particle in the x, y, and z directions. Thus the overall shape can be characterised by the two aspect ratios a/b and a/c. The parameter e expresses the roundness of the particle in the azimuthal direction, while n controls the roundness in the polar direction. We mostly focus on cubic superellipsoids, which are characterised by $a/b = a/c = 1$ and $0 \leq n \leq 1$, $0 \leq e \leq 1$. For simplicity, we also assume $n = e$. We perform computations for the same sizes and salt-mass fractions as for the reference model, as well as for $n = e$ =0.1, 0.2, …, 0.9. The

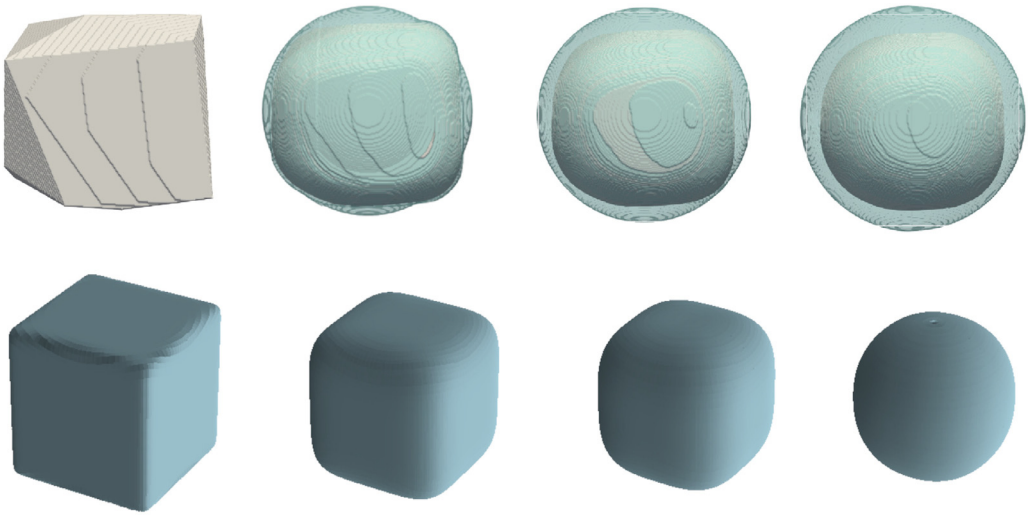

Fig. 1. Top row: Selected geometries illustrating the reference model for marine aerosols with sea-salt mass fractions (from left to right) f_m=1.00, 0.97, 0.94 and 0.91. Bottom row: Cubic superellipsoids with roundness parameters (from left to right) $e = n$ =0.1, 0.4, 0.6, 0.9.

mass fraction determines the volume-equivalent wet radius of the particles (as explained in the appendix). Since the superellipsoids are homogeneous particles, the impact of the inhomogeneous salt core/brine mantle morphology on the optical properties is not accounted for in this model. Rather, we compute the optical properties of the homogeneous superellipsoids by use of a complex effective refractive index, which is computed from the volume fraction and from the complex refractive indices of the salt core and the brine mantle; this is done by use of the Maxwell-Garnett rule [36]. The volume fraction is computed from the mass fraction as detailed in the appendix.

2.2. Numerical computation of aerosol optical properties

For the reference particles, the electromagnetic scattering problem is solved by use of the discrete-dipole approximation (DDA). The DDA is based on the volume-integral equation, which can be derived from Maxwell's equations (e.g. [37]). The volume of the particle is discretised into a grid of polarisable cells. By making the cells much smaller than the wavelength, one can assume that all points in a cell oscillate in phase, just like a dipole. The volume-integral can thus be converted into a system of linear equations, which can be solved numerically. We employ the DDA code ADDA version 1.3b4 [38]. The size of the spacial grid, i.e., the dipole spacing d, needs to be chosen judiciously. We have previously performed tests that showed that a dipole spacing satisfying $|m|kd \lesssim 0.4$ is more than sufficient for sea-salt model particles [19]. For this choice of dipole spacing, comparisons for superellipsoids showed excellent agreement between DDA and T-matrix results computed with the Tsym code [39].

The particles are assumed to be randomly oriented. In ADDA orientation-averaged results are obtained by Romberg integration over the three Euler angles α, β, γ. For each angle a range of values and a range of subdivisions $J_{\min}$, $J_{\max}$ is set. Following the sensitivity study in [19], we use $J_{\min} = 2$, $J_{\max} = 4$ within the range $[0, 360^\circ]$ for α and γ, and $J_{\min} = 2$, $J_{\max} = 3$ within the range $[0, 180^\circ]$ for β. For more information on how the choice of d and the number of Euler angles affects the accuracy of the computations we refer to [19].

The optical properties of superellipsoids are computed by use of the T-matrix program Tsym [39], version 6.6, which is based on Waterman's null-field method [40]. The program accounts for particle symmetries by using commutation relations of the T-matrix [21,41] and irreducible representations of the particle's symmetry group [42]. Orientation averaged optical properties can be derived analytically [43,44]. The use of symmetries and of analytical orientation averaging are the two main advantages of T-matrix methods [37]. To apply the method to superellipsoids requires us to re-express the implicit equation given in (3) as an explicit parameterisation of the particle surface in spherical coordinates. A derivation of this surface parameterisation and its partial derivatives can be found in [18].

The DDA and T-matrix computations were run on the Bi cluster of the Swedish National Supercomputer Centre, which uses 8-core Intel Xeon E5-2640v3 processors at 2.6 GHz. For each of the reference particles we used between 1–8 nodes (depending on size), where each node contains 16 cores with 64 GB memory. The ADDA computations alone took slightly more than two months of wall-clock time. The T-matrix computations only took a few hours on a single core.

Post-processing of the ADDA and Tsym output involved the computation of ensemble-averaged optical properties. We are mainly interested in quantities relevant for lidar remote-sensing applications, namely, the extinction cross section C_{ext}, the backscattering cross section C_{bak}, and the linear backscattering depolarisation ratio δ_L. $C_{\text{ext}} = C_{\text{sca}} + C_{\text{abs}}$ is the sum of the scattering and absorption cross sections. The scattering cross section C_{sca} of a single particle at a given wavelength is defined as the total monochromatic power removed by scattering from the incident wave divided by the incident energy flux. The absorption cross section C_{abs} is defined analogously. The backscattering cross section is defined by

$$C_{\text{bak}} = \frac{1}{4\pi} C_{\text{sca}} F_{11}(180^\circ), \tag{4}$$

where the phase function $F_{11}(\Theta)$ is the first element of the normalised Mueller matrix $F_{ij}(\Theta)$. The elements of this matrix are functions of the scattering angle Θ. They express the relation between the Stokes vector components I, Q, U, V of the incident and the scattered electromagnetic fields far away from the scatterer, i.e.

$$\begin{pmatrix} I_s \\ Q_s \\ U_s \\ V_s \end{pmatrix} = \frac{C_{\text{sca}}}{4\pi r^2} \begin{pmatrix} F_{11} & F_{12} & F_{13} & F_{14} \\ F_{21} & F_{22} & F_{23} & F_{24} \\ F_{31} & F_{32} & F_{33} & F_{34} \\ F_{41} & F_{42} & F_{43} & F_{44} \end{pmatrix} \cdot \begin{pmatrix} I_i \\ Q_i \\ U_i \\ V_i \end{pmatrix}, \tag{5}$$

where r denotes the distance from the scatterer, and the subscripts i and s label the incident and scattered Stokes-vector components.

The linear depolarisation ratio (LDR) in the backscattering direction is defined by

$$\delta_L = \left.\frac{F_{11}-F_{22}}{F_{11}+F_{22}}\right|_{\Theta=180^\circ}. \tag{6}$$

Another derived quantity of interest is the extinction-to-backscattering ratio S, also known as the lidar ratio

$$S = \frac{C_{\rm ext}}{C_{\rm bak}}. \tag{7}$$

When computing ensemble-averaged optical properties, such as averages over a size-distribution $n(r)$, one computes ensemble-averaged cross sections

$$\bar{C}_{\rm sca} = \frac{\int {\rm d}r n(r) C_{\rm sca}(r)}{\int {\rm d}r n(r)} \tag{8}$$

(and similarly for $\bar{C}_{\rm abs}$), and the ensemble-averaged Mueller matrix

$$\bar{F}_{ij}(\Theta) = \frac{\int {\rm d}r n(r) C_{\rm sca}(r) F_{ij}(r;\Theta)}{\int {\rm d}r C_{\rm sca}(r) n(r)}. \tag{9}$$

The ensemble-averaged Mueller matrix is often denoted as the Stokes scattering matrix [45]. Substitution of ensemble-averaged quantities into Eqs. (4), (6), and (7) yields the corresponding ensemble-averaged backscattering cross section $\bar{C}_{\rm bak}$, LDR $\bar{\delta}_L$, and lidar ratio $\bar{S}$.

2.3. Size distributions

The size-distribution of atmospheric aerosols is often described by a lognormal size distribution given by

$$n(r) = \frac{N_0}{r \ln\sigma_g \sqrt{2\pi}} \exp\left[-\frac{\ln^2(r/r_{\rm med})}{2\ln^2\sigma_g}\right], \tag{10}$$

where N_0 denotes the number of particles per unit volume of air, $r_{\rm med}$ is the median volume-equivalent particle radius, σ_g denotes the geometric standard deviation, and ln is the natural logarithm. $n(r){\rm d}r$ is the number of particles per unit volume of air within a radius interval $[r, r+{\rm d}r]$. The size distribution of marine aerosols has also been modelled by use of bimodal lognormal distributions [46], i.e., by the sum of two lognormal distributions. However, inspection of measured size distributions of marine aerosols rarely shows two well-separated modes (e.g. [46]). It appears that this model has mainly been introduced to conveniently describe relatively broad size distributions that are not well fitted by a mono-modal lognormal function. The price one pays for a better fit is that one doubles the number of free parameters compared to a mono-modal lognormal function. This makes this model rather unattractive for size-retrieval problems, as it is unlikely that one can constrain all six free parameters of a bi-lognormal distribution with remote sensing observations.

In chemical transport models (CTMs) different models for the size distribution of marine aerosols have been developed. For instance, in [8] a size distribution is used of the form

$$n(r) = N_1 \frac{\exp\left(\frac{-0.09}{2r+0.003}\right)}{2+\exp\left(\frac{-5}{2r}\right)} \cdot \frac{1+0.05(2r)^{1.05}}{(2r)^3} \cdot 10^{1.05\exp\left[-\left(\frac{0.27-\log(2r)}{1.1}\right)^2\right]} \cdot (2r)^{-\alpha}. \tag{11}$$

In this parameterisation, the particles' volume-equivalent radius r is given in μm. N_1 is a factor that is proportional to the total number density of particles. In CTMs, the number density (or the flux of particles from water to air) is modelled as a function of horizontal wind speed 10 m above the water surface, sea-surface temperature (SST), and salinity S_a. The exponent α is modelled as a function of SST and S_a. Typical values of α lie between 0 and 1, but for low values of the salinity it can be almost as large as 3. It increases with decreasing SST and with decreasing S_a. The detailed relations can be found in [8]. The model given in Eq. (11) is a synthesis of two earlier models that were based on observations of bubble-bursting and spume drops [47] and of laboratory measurements in a bubble chamber[48]. The measurements by [48] covered the particle-radius range from 0.01–10.0μm, where particle radii between 0.01–0.069μm were observed in 11 size bins by a differential mobility particle sizer, and those between 0.069–10.0μm were measured in 30 size channels by an optical particle counter. Thus the parametrisation in [8] is based on reasonably realistic laboratory proxies observed over a large size range with high size resolution. This parametrisation is currently being employed, e.g., in the latest versions of the chemical transport models MATCH [49], SILAM [8], and EMEP [50], all of which are members of the European Copernicus Air-quality forecasting ensemble (https://atmosphere.copernicus.eu/air-quality). Evaluations of the emission scheme in conjunction with CTMs comprise comparison with in situ size distribution measurements [8,51], as well as in situ measurements of mass concentration in air and wet deposition of sea salt [4].

Fig. 2 shows some examples of the lognormal size distribution (top) for σ_g=1.5, and for $r_{\rm med}$=0.1 (black), 0.3 (red), and 0.7 μm (green). The bottom panel shows the modified power-law distributions defined in Eq. (11) for α=0.1 (black), 1.5 (red), and 3.0 (green). The lognormal distribution is a rather generic size distribution that covers a very wide spectrum from particle populations that are strongly dominated by small particles to those that mainly consist of large particles. By contrast, the size distribution given in Eq. (11) describes a fairly broad distribution with a high fraction of small particles. Since this modified power-law distribution is based on observations, it can be considered to be a reasonably realistic model for marine aerosols. In our study we consider both cases. The lognormal distribution is used with a fixed value of σ_g=1.5, and with $r_{\rm med}$ ranging from 0.1 to 1.1 in steps of 0.1. The modified power-law distribution in Eq. (11) is used with α varying between 0.0 and 3.0 in steps of 0.3.

3. Results

Fig. 3 presents $C_{\rm ext}$ (top left), $C_{\rm bak}$ (top right), S (bottom left), and δ_L (bottom right) prior to computing an ensemble-average. The x-axis shows the volume-equivalent radius of the dry salt particle prior to adding liquid water. The four curves represent salt mass-fractions f_m=1.00 (pure salt, black), 0.97 (blue), 0.94 (red), and 0.91 (green). The fluctuations of the optical properties as a function of size are caused by resonances of the field induced in the particles, but also by the stochastic variations in our model geometries. The amplitude of these fluctuations is generally larger for differential scattering properties, such as $C_{\rm bak}$ and δ_L, than for integral optical properties, such as $C_{\rm ext}$.

Computation of ensemble-averaged quantities smooths out much of these fluctuations and reduces the range within which each optical property varies. Fig. 4 presents optical properties averaged over a lognormal size distribution. The panels and colours are as in Fig. 3. The top scale on the x-axis shows the median dry radius $r_{\rm med}^{\rm dry}$. For pure salt particles ($f_m = 1.0$) this is equal to the median radius $r_{\rm med}$ in Eq. (10). For water-coated particles ($f_m < 1.0$), it is equal to the median radius $r_{\rm med}$ of the size distribution that one would obtain by removing all the water. Thus, it is important to understand that in this figure we are comparing ensembles of different sizes. As we go from $f_m = 1.00$ to $f_m = 0.91$, addition of an increasing amount of water results in a shift of the entire size distribution to larger sizes. The advantage of presenting the results as a function of $r_{\rm med}^{\rm dry}$ is that we very clearly see the effect of the addition of water on the cross sections.

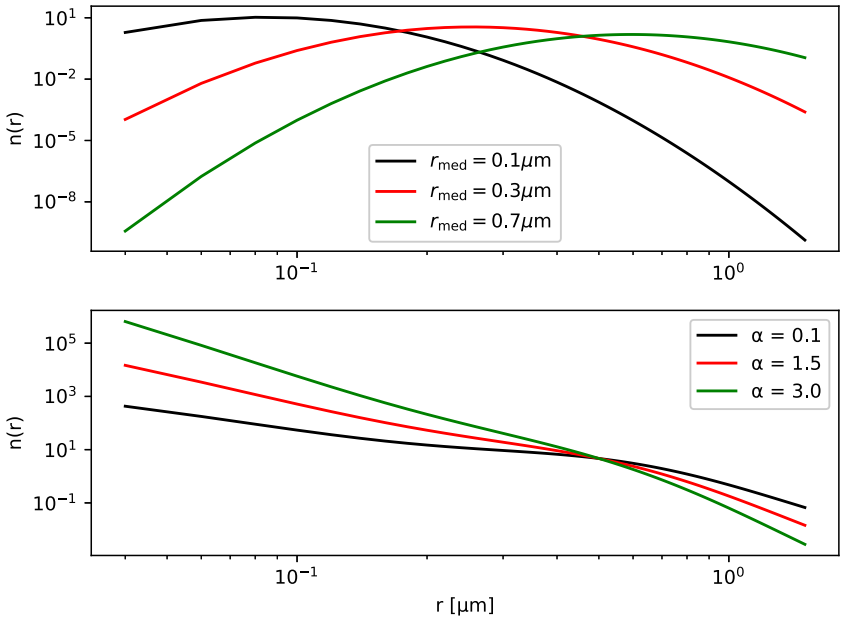

Fig. 2. Top: lognormal size distributions for three different values of the median radius. Bottom: modified power-law distributions for three different values of the slope-parameter α.

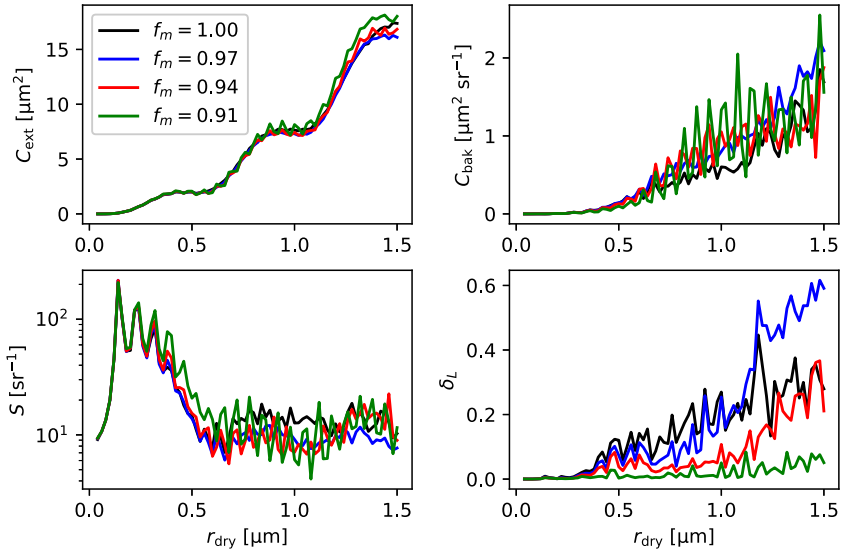

Fig. 3. Results obtained for the reference model of brine-coated convex salt polyhedra: C_{ext} (top left), C_{bak} (top right), lidar ratio S, and LDR δ_L as a function of the dry radius prior to size averaging. Results are shown for four values of the salt-mass fraction f_m, where $f_m = 1$ refers to pure salt.

The bottom x-axis shows the effective dry radius

$$r_{\text{eff}}^{\text{dry}} = \frac{\int n(r)r\pi r^2 \mathrm{d}r}{\int n(r)\pi r^2 \mathrm{d}r}, \tag{12}$$

where $n(r)$ has a median radius $r_{\text{med}}^{\text{dry}}$. The effective radius is based on weighing $n(r)r$ with a mean geometric cross sectional area πr^2. In the geometric optics regime, where the absorption and scattering cross sections are proportional to the geometric cross section, this provides an accurate measure for the mean particle size contributing to the size-averaged cross sections. In the resonance regime (also referred to as the Mie regime), where the particle radii are comparable to the wavelength of light, the dependence of the cross sections on particle radius can be quite complex, which makes it difficult to define an analogous measure. However, the effective radius as defined in Eq. (12) is still being used as a proxy for estimating the mean optical size of the particles. For us, the motivation for introducing $r_{\text{eff}}^{\text{dry}}$ is to have a common size measure that allows us to compare the results obtained with the lognormal and the modified power-law size distributions.

The addition of water has a minor effect on $\bar{C}_{\text{ext}}$ (top left), but a stronger effect on $\bar{C}_{\text{bak}}$ (top right). For instance, for $r_{\text{med}}^{\text{dry}}$=1.1$\mu$m a reduction of f_m from 1.0 to 0.91 increases $\bar{C}_{\text{ext}}$ from 8.4 to 8.8 μm^2, while $\bar{C}_{\text{bak}}$ increases from 0.65 to 0.89 μm^{2}sr^{-1}. $\bar{\delta}_L$ depends as much on size as on the salt mass fraction. In fact, it is the quantity that is most sensitive to changes in f_m. For $r_{\text{med}}^{\text{dry}}$=1.1$\mu$m it varies between 0.03 and 0.31, where the peak values are attained for $f_m = 0.97$. The lidar ratio $\bar{S}$ is mainly depending on particle size. For $r_{\text{med}}^{\text{dry}}$=0.1$\mu$m it can exceed 60 sr, while for $r_{\text{med}}^{\text{dry}}$=1.1$\mu$m it can be as low as 10 sr.

Fig. 5 presents analogous results for the modified power-law distribution in Eq. (11). The top x-axis shows the exponent α that controls the slope of the size distribution, while the bottom x-axis

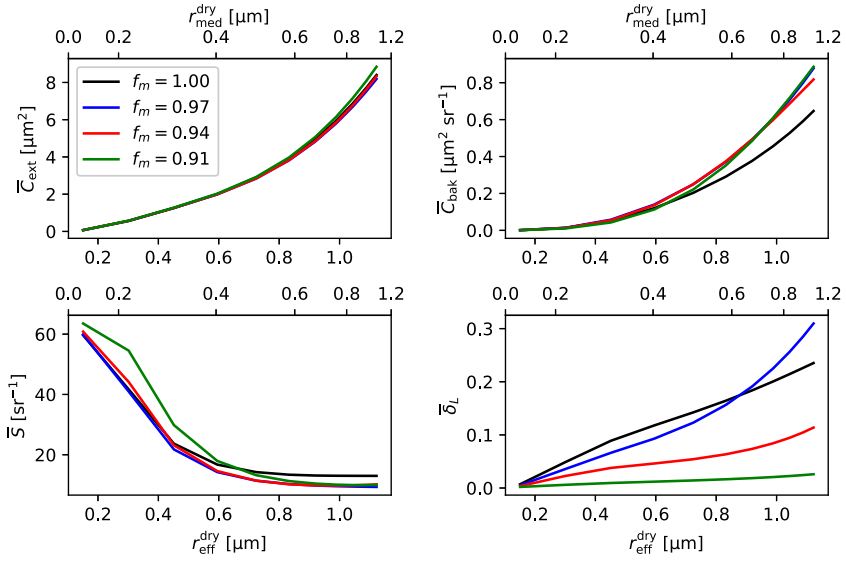

Fig. 4. As Fig. 3, but averaged over lognormal size-shape distributions. The x-axis shows the effective dry radius (bottom scale) and the corresponding median dry radius (top scale).

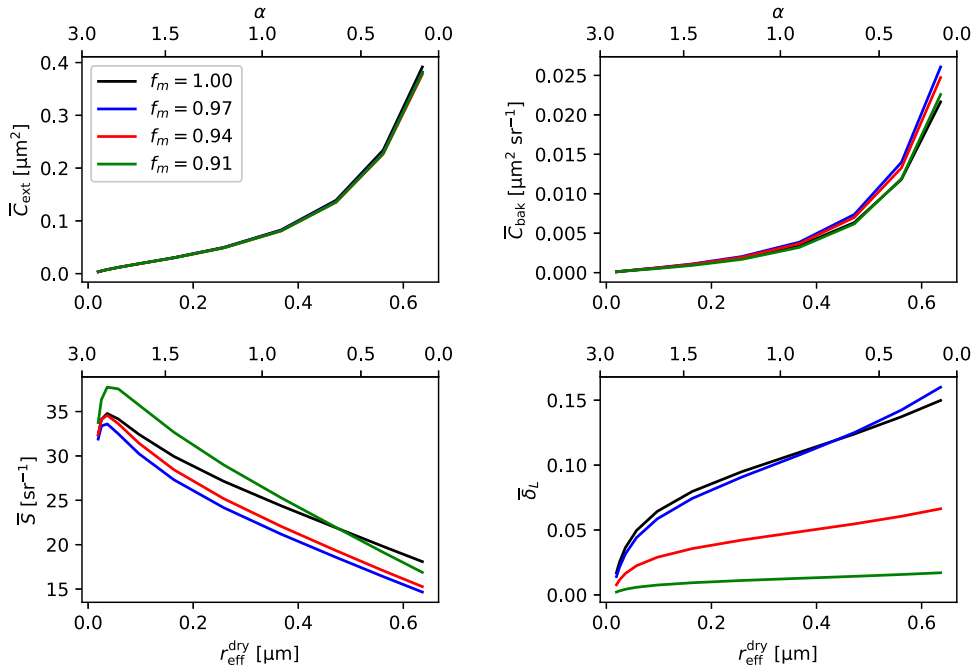

Fig. 5. As Fig. 4, but averaged over modified power-law size-shape distributions. The bottom x-scale is as before, the top x-scale shows the slope parameter α.

shows the corresponding effective dry radius. We observe only minor differences in $\bar{C}_{ext}$ (top left) between ensembles of dry and wet particles. $\bar{C}_{bak}$ (top right) is more sensitive to f_m, especially for ensembles with higher values of r_{eff}^{dry} and lower values of α. For $\alpha = 0.0$ and $f_m = 1.0$, we have $\bar{C}_{bak}$=0.022 μm^{2}sr^{-1}. As more water is added (i.e., f_m is being reduced), there is an initial increase in $\bar{C}_{bak}$ to 0.026 μm^{2}sr^{-1}, followed by a gradual decrease. $\bar{\delta}_L$ (bottom right) is highly sensitive to both size and mass fraction. For $\alpha = 0.0$, we have peak values for thinly water-coated particles ($f_m = 0.97$) of $\bar{\delta}_L$=0.16. As more water is added and more salt is dissolved in the coating, the particle becomes more spherical. This strongly quenches the LDR; $\bar{\delta}_L$ decreases to 0.02 at f_m=0.91.

Comparison between the bottom right panels in Figs. 4 and 5 reveals that for comparable values of r_{eff}^{dry} the LDR varies within similar ranges for either size distribution. More pronounced differences between Fig. 4 and 5 are observed for the lidar ratio (bottom left), especially for low values of r_{eff}^{dry}. While the lognormal size distribution yields values of $\bar{S}$ exceeding 60 sr, the corresponding results in the modified power-law distribution remain below 40 sr. Finally, for comparable values of r_{eff}^{dry} the lognormal distribution yields significantly higher cross sections (Fig. 4, top row) than the power-law distribution (Fig. 5, top row). This mainly confirms that size-averaged optical cross sections in the resonance regime can strongly depend on the entire size distribution, not just on its effective radius.

To further illustrate the reference model's characteristics, we compare it to a symmetric, homogeneous model, namely, cubic superellipsoids. Fig. 6 shows results for a mass fraction $f_m = 0.97$ and a modified power-law size distribution. Thus, these results should be compared with the blue lines in Fig. 5. Each panel shows opti-

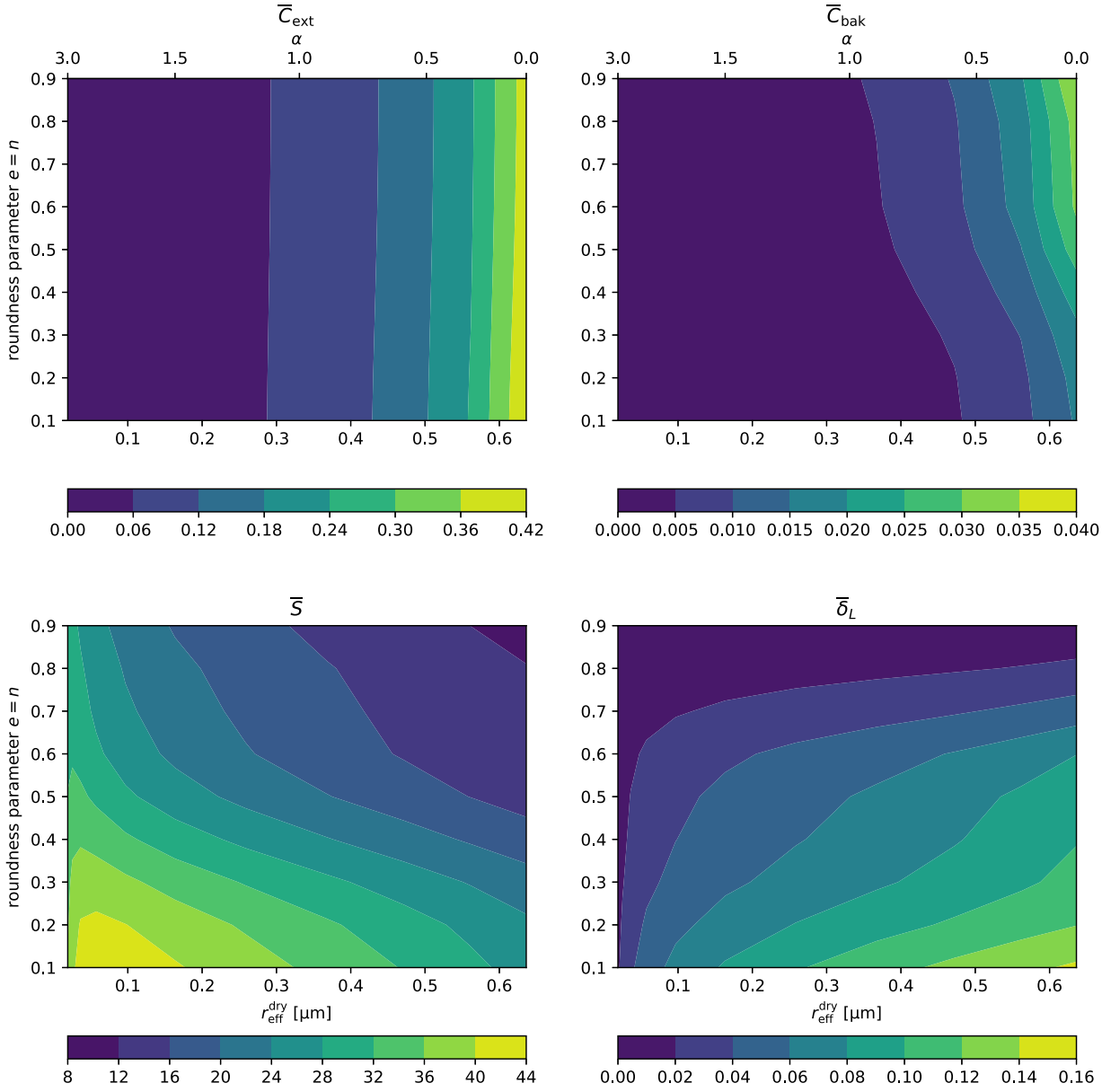

Fig. 6. Results obtained for cubic superellipsoids, averaged over a modified power-law size distributions, and assuming f_m=0.97: $\bar{C}_{ext}$ (top left), $\bar{C}_{bak}$ (top right), lidar ratio $\bar{S}$, and LDR $\bar{\delta}_L$. The x-axis shows the effective dry radius (bottom scale) and the slope parameter α (top scale), the y-axis shows the roundness parameter $e = n$.

cal properties computed with superellipsoids as a function of r_{eff}^{dry} (bottom x-scale) or exponent α (top x-scale) and of the roundness parameter $e = n$ on the y-axis. $\bar{C}_{ext}$ (top left) is insensitive to the shape and depends only on size. These results largely agree with those obtained for the reference model in Fig. 5. The size dependence of $\bar{C}_{bak}$ (top right) shows qualitatively the same steep increase at larger values of r_{eff}^{dry} for both models, while the lidar ratio $\bar{S}$ decreases with growing r_{eff}^{dry}. Best agreement with the reference model is achieved for a roundness parameter of about 0.6. It is interesting to note that $\bar{C}_{bak}$ is just slightly more sensitive to the roundness parameter than $\bar{C}_{ext}$. But this small difference results in a pronounced shape-dependence of $\bar{S}$. The LDR $\bar{\delta}_L$ (bottom right) has a distinct size dependence, but an even stronger shape dependence. The maximum values are around $\bar{\delta}_L$ =0.16, which is on the same order as the reference model. However, the superellipsoids have such high LDR values only for $e = n = 0.1$, which corresponds to particles with only mildly rounded edges and corners.

We repeated these computations for superellipsoids with other values of the salt-mass fraction f_m, which entails small adjustments in the size distribution and the complex refractive index. The resulting optical properties (not shown) deviate little from those shown in Fig. 6. We also repeated all computations for superellipsoids with an aspect ratio $c/a = 1.25$, which corresponds to more elongated bricks with rounded edges. The results are shown in Fig. 7. Compared to the cubic particles in Fig. 6 (c/a=1) the extinction cross section is hardly affected by the elongation, while the backscattering cross section is reduced by about 20%. The LDR is increased by roughly a factor of 2. Also, while for cubic superellipsoids LDR was close to zero for a roundness parameter $e = n = 0.9$, the elongated superellipsoids have substantially higher values up to 0.36.

Finally, we repeated the size averaging by using our lognormal distribution instead of the modified power-law distribution. As before, we assumed $\sigma_g = 1.5$.

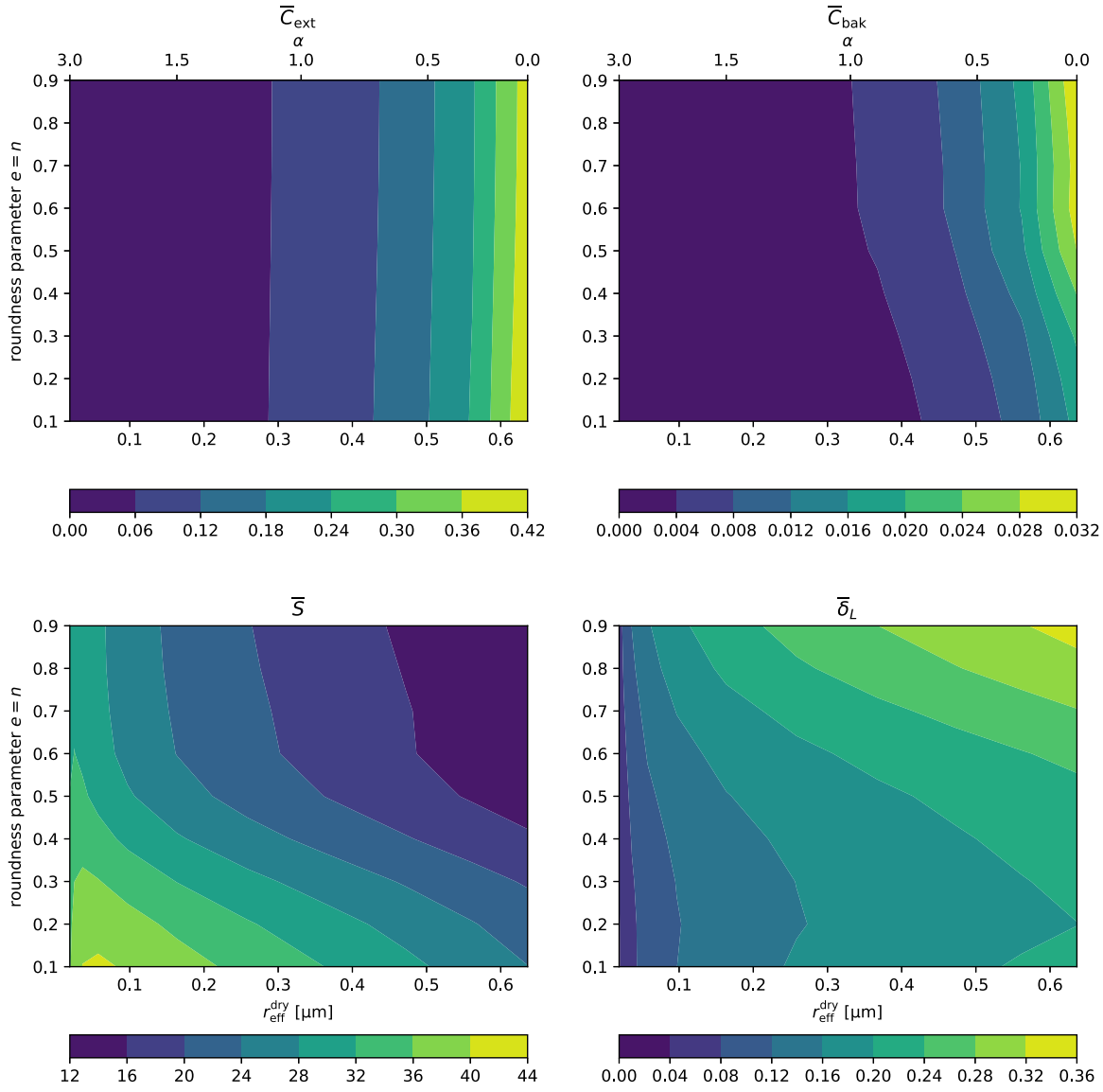

Fig. 7. As Fig. 6, but for elongated superellipsoids with aspect ratios b/a=1 and c/a=1.25.

The results are shown in Fig. 8. The extinction and backscattering cross sections (top row) are generally higher compared to the corresponding results for the modified power-law distribution in Fig. 6. For instance, for $r_{\rm eff}^{\rm dry} = 0.6\,\mu$m and $e = n = 0.9$, the lognormal distribution yields $\bar{C}_{\rm ext} = 2.0\,\mu{\rm m}^2$ and $\bar{C}_{\rm bak} = 0.23\,\mu{\rm m}^2\,{\rm sr}^{-1}$. The corresponding values for the power-law distribution are $\bar{C}_{\rm ext} = 0.28\,\mu{\rm m}^2$ and $\bar{C}_{\rm bak} = 0.024\,\mu{\rm m}^2\,{\rm sr}^{-1}$. We observed a comparable sensitivity of the cross sections to the choice of size distribution for the reference model. For $r_{\rm eff}^{\rm dry} = 0.6\,\mu$m, the lidar ratio (bottom left) varies with the roundness parameter for the lognormal size distribution in Fig. 8 between S=12–29 sr, and the LDR varies between 0–0.15. The corresponding ranges for the power-law size distribution in Fig. 6, are for the lidar ratio between 9–28 sr, and for the LDR between 0–0.14, which is of comparable magnitude.

Comparison of the lognormal distributions of the superellipsoids (Fig. 8) and the reference model (blue lines in Fig. 4) shows, that the cross sections and the lidar ratio of both models agree well, especially with superellipsoids with $e = n$ around 0.6. However, for $r_{\rm eff}^{\rm dry} \geq 1\mu$m, the reference model yields LDR values as high as 0.3, while the homogeneous cubic superellipsoids give LDR values not much higher than 0.2. However, as we saw in Fig. 7, when making the superellipsoids even slightly elongated, one can produce much higher LDR values with this model.

The differences and similarities between the reference and the homogeneous superellipsoid models can be seen more distinctly when plotting results for monodisperse rather than size-averaged optical properties.

Fig. 9 shows results for a mass fraction of f_m=0.97 for the reference model (solid line) and for cubic, homogeneous superellipsoids (dashed lines, $a/c = a/b = 1$) with different roundness parameters as indicated in the legend. For this mass fraction, superellipsoids with a roundness parameter of $e = n$ =0.6 give the most faithful fit of the size-dependence of $C_{\rm ext}$, $C_{\rm bak}$, and S computed with the reference model. However, for $r_{\rm dry} > 1\mu$m, all instances of the superellipsoid model predict LDR values that are lower than that of the reference model.

Fig. 10 shows analogous results for a mass fraction of f_m=0.91. As for f_m =0.97, homogeneous cubic superellipsoids with a roundness parameter of $e = n$ =0.6 show the best agreement with the reference model for the cross sections and the lidar ratio. However,

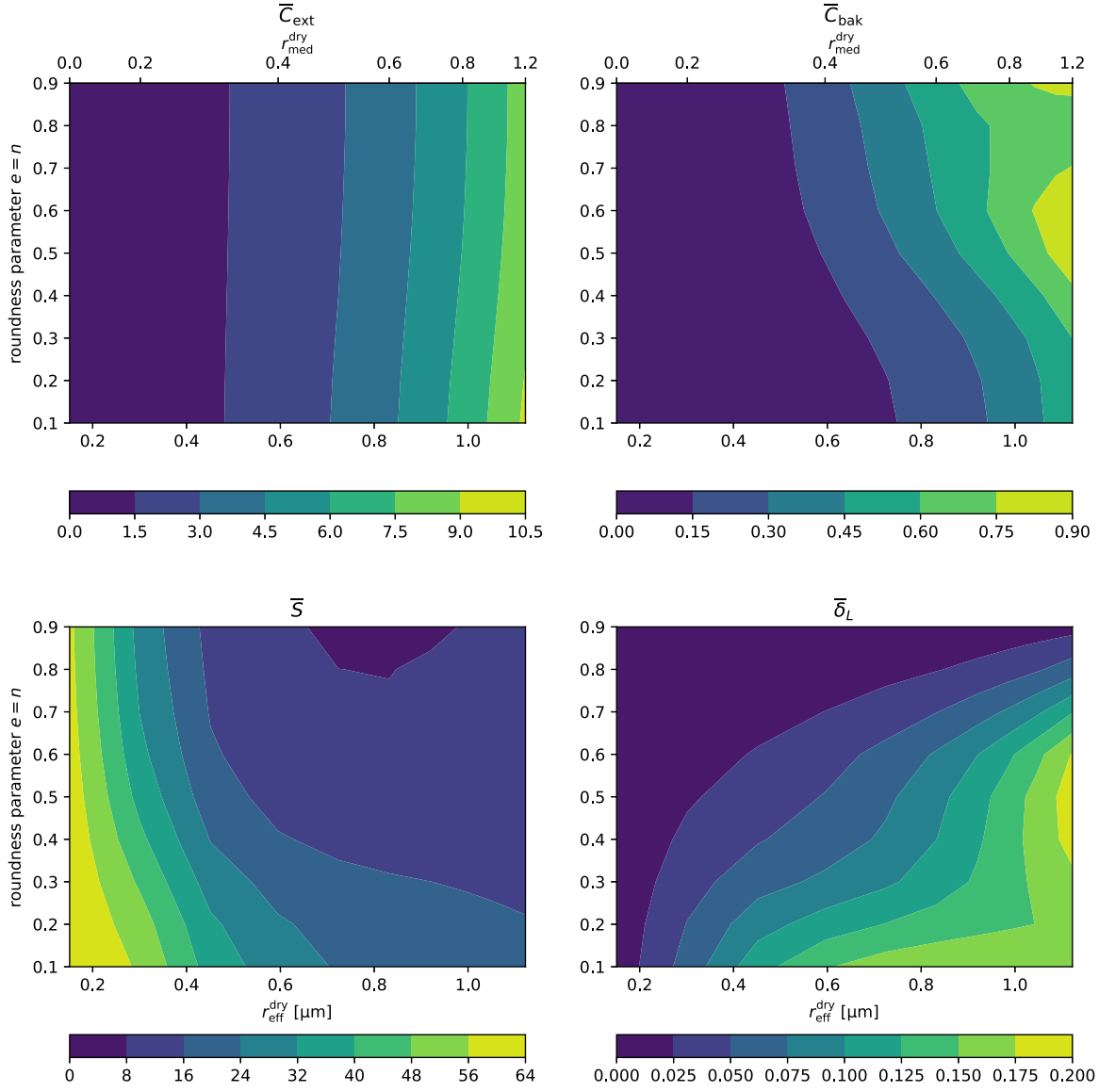

Fig. 8. Analogous to Fig. 6, but averaged over lognormal size distributions. The upper axis on the x-axis shows the median dry radius of the lognormal distribution.

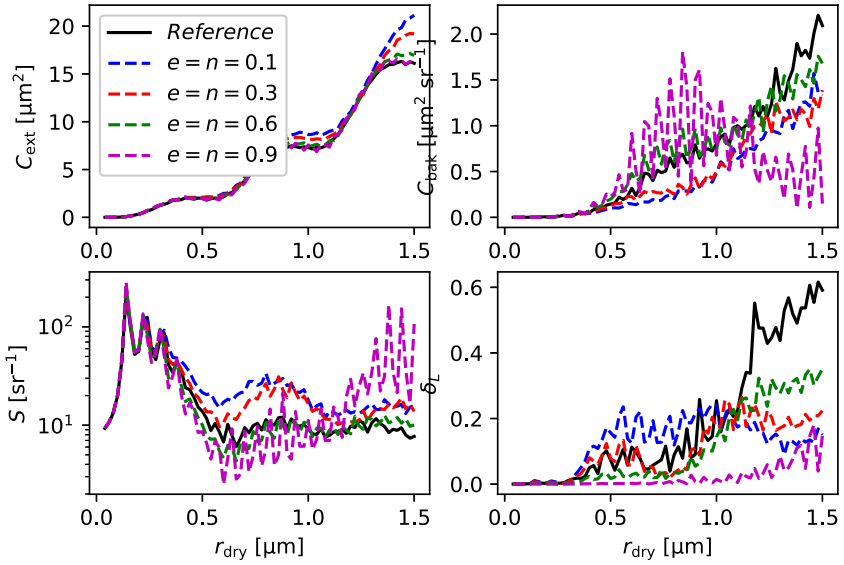

Fig. 9. Model comparison for a mass fraction of f_m=0.97: C_{ext} (top left), C_{bak} (top right), lidar ratio S, and LDR δ_L, for monodisperse particles as a function of the dry radius. The curves represent the reference model (black solid), and superellipsoids (dashed lines) with roundness parameters 0.1 (blue), 0.3 (red), 0.6 (green), and 0.9 (magenta).

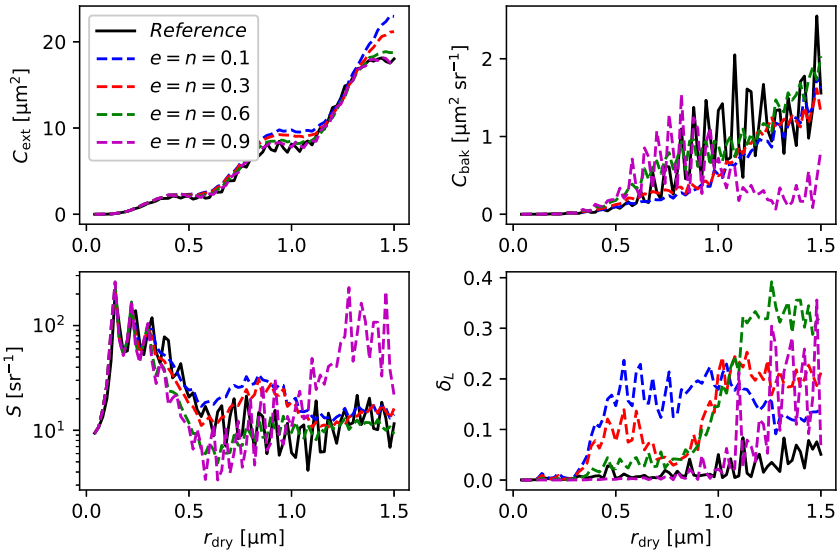

Fig. 10. Analogous to Fig. 9, but for a mass fraction f_m=0.91.

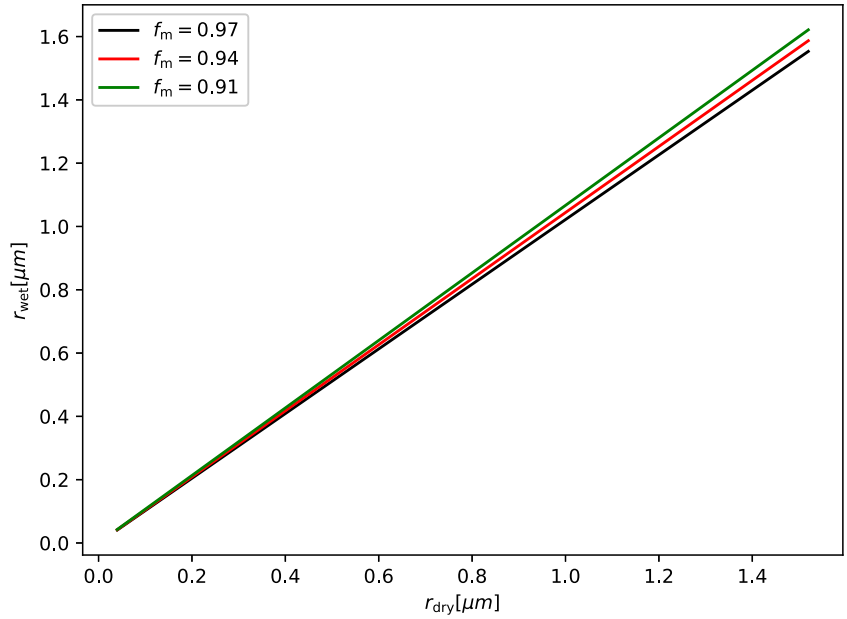

Fig. 11. Volume-equivalent wet radius for three different salt-mass fractions as a function of volume-equivalent dry radius according to Eq. (A.8).

for $r_{\rm dry} \geq 1\mu$m, all instances of the homogeneous cubic superellipsoids give LDR values that lie in the range 0.1–0.4, while the reference model never exceeds 0.1. This confirms that even mildly aspherical homogeneous particles can produce significant depolarisation, a fact that is well known from studies on spheroids [52]. By contrast, the inhomogeneous reference model yields depolarisation results that are more strongly quenched as the particles become more rounded due to water adsorption. To reproduce the LDR reference results with cubic homogeneous superellipsoids, one would likely need to use a roundness parameter exceeding 0.9. However, this would most likely reduce the agreement between the two models for $C_{\rm bak}$ and S.

4. Discussion

Fig. 11 shows the volume-equivalent wet radius of our model particles as a function of the volume-equivalent dry radius of the bare salt particle for three different values of the salt mass fraction f_m. (The detailed relation is given in the appendix.) For instance, for $r_{\rm dry}$=1.5μm and f_m=0.91, the corresponding wet radius is $r_{\rm wet}$=1.6μm. Thus, within the range of mass fractions considered here, the addition of water has only a minor effect on particle size. This explains why $\bar{C}_{\rm ext}$ in Figs. 4 and 5 (top left) is not very sensitive to changes in f_m. The high sensitivity of $\bar{\delta}_L$ to f_m (bottom right) can be entirely attributed to changes in particle morphology. For f_m=0.91, the liquid mantle of the model particles is more or less spherical (Fig. 1 right). This strongly suppresses depolarisation in the backscattering direction, which is evident in both Figs. 4 and 5.

Incidentally, it is not straightforward to relate the mass fractions to the ambient relative humidity. Fig. 7 in [7] provides the efflorescence and deliquescence curves of sea salt. A visual inspection in conjunction with Eq. (A.8) in our appendix shows that our range of mass fractions $0.91 \leq f_m \leq 1.0$ corresponds to relative humidities of roughly 43–48% on the efflorescence branch, and 60–72% on the deliquescence branch of the curve. But note that the results in [7] are based on laboratory measurements by [53]. Field measurements of lidar depolarisation ratios can give some indirect

evidence on the transition from nonspherical dry crystals to spherical liquid droplets [24,54,55]. The results shown in [24] (Fig. 13 in that paper) show a rather weak hysteresis effect and a remarkably smooth transition from $\bar{\delta}_l \sim 0.1$ around RH∼40% to $\bar{\delta}_l \sim 0$ at RH≥80%. The analysis in [55] of ten years of night time CALIPSO data during Austral winter over the Southern Ocean shows no conclusive evidence for the hysteresis effect, and a fairly smooth transition from $\bar{\delta}_l \sim 0.14$ at RH=40% to $\bar{\delta}_l \sim 0.06$ as RH approaches 100%. This raises the question whether in nature the hysteresis effect is weaker and the transition from dry crystals to wet droplets is more gradual than suggested by laboratory studies.

How realistic are the results of our reference model quantitatively? In [18] a review of recent field measurements can be found (see Table 1 in that paper). At a wavelength of 532 nm, LDR values ranging from 0.01 to 0.29 have been reported, but most observed values are lower than 0.2. Typical values of the lidar ratio $\bar{S}$ are between 15 and 30 sr. Our computations with the modified power-law distribution (Fig. 5) results in LDR values and lidar ratios that are overall consistent with the majority of field observations for the entire range of the slope parameter α. Specifically, for relatively dry particles with $f_m \geq 0.97$ and for α between 0 and 1 (typical over the oceans) we obtain LDR values between 0.1 and 0.15. This is also consistent with findings in the climatology study of CALIPSO data over the Southern Ocean mentioned above [55]. The lognormal size distribution (Fig. 4) yields a larger range of lidar ratios between 10–60, and LDR values between 0–0.3. This is to be expected, since the motivation of investigating this size distribution was to cover a fairly broad range of effective radii, which yields a correspondingly large range of optical properties. Results that are consistent with the majority of the field observations reviewed in [18] are obtained for a range of median radii of about $0.4\,\mu\text{m} \leq r_{\text{med}}^{\text{dry}} \leq 0.8\,\mu\text{m}$.

Recall that our computations were limited to particles with a maximum volume-equivalent radius of r_{V}=1.5μm. Ensembles of marine aerosols in nature can contain larger particles. For instance, [48] measured the size distribution of sea salt particles generated in a bubble chamber for particle radii up to 10μm. But results are presented in that paper only for particle radii up to 5μm. Larger particles are only encountered in very low number concentrations. If we were able to include particles in the range 1.5–5.0μm in our model, then the effective radius of the size distribution would increase. For instance, with our cut-off radius of 1.5μm, the power-law size distribution covers a range of effective radii of 0.019–0.64μm. Extending the cut-off radius to 5.0μm will increase the maximum effective radius to 0.90μm. This may modulate the results. In particular, it could lead to an increase in the LDR.

Cross sections and lidar ratios computed with the cubic homogeneous superellipsoid model (Figs. 6 – 10) agreed best with the reference model for a roundness parameter around $e = n = 0.6$. For thinly water-coated aerosols (e.g. $f_m = 0.97$ in Fig. 9), the cubic homogeneous superellipsoids yield LDR values that are lower than those of the reference model, while for $f_m = 0.91$ (Fig. 10) the reference results are generally lower. This suggests that in order to reproduce the reference results, one should relax some of the constraints we have imposed on the superellipsoids. One possibility is to allow the superellipsoids to become elongated. It has been shown in [17] that changing the roundness parameter results in substantial changes in the LDR. Our results in Fig. 7 are consistent with this. By changing the aspect ratio from $c/a = 1$ to $c/a = 1.25$, the maximum LDR values obtained over the range of considered roundness parameters and effective particle radii has been extended from 0.16 to 0.36. The other possible extension of the homogeneous superellipsoid model is to consider inhomogeneous superellipsoids, as was done in [17,18]. One advantage of inhomogeneous superellipsoids is that they are morphologically quite realistic. Inhomogeneity is known to be an important cause of depolarisation [56], but also of other optical effects. For instance, even with a particle model as flexible as spheroids it has been found that homogeneous spheroids are not always adequate to reproduce optical properties of corresponding inhomogeneous spheroids [57]. It has also been shown by use of eccentric spherical core-mantle model particles that off-centre positioning of a spherical salt core inside a spherical brine mantle can give rise to considerable depolarisation [18]. On the other hand, one advantage of elongated homogeneous superellipsoids is that their optical properties can be computed with the null-field method (e.g. [19]), which is computationally fast.

5. Conclusions

The main purpose of this work was to propose and test a class of model particles that can be used as a reference model for simulating optical properties of marine aerosols. The approach is based on a pseudo-potential model that is designed to mimic the processes of water adsorption, solution of salt, and rearrangement of the brine mantle. One main tuning parameter is the thickness of the liquid surface layer that remains fixed during the rearrangement process. In a predecessor of our model [18], this process was absent, which corresponds to a surface-layer thickness equal to the mantle thickness. That model instance can give LDR values that are only slowly converging to zero as more water is being added, since the particles transit very gradually from cubic to spherical shape. Here, we test the extended model by setting the surface-layer thickness to a rather low value of 3d, where d is the dipole spacing in the DDA. By contrast to the findings in [18], this model instance gives a rather rapid transition from high LDR to low LDR values. At a mass fraction of f_m=0.91 the LDR was already reduced to 0.02 or less, depending on the median radius. This may be too rapid a transition from high to low values of LDR. But without further guidance from more detailed laboratory measurements, it is difficult to know exactly what choice of the surface-layer thickness yields the most realistic description of LDR-quenching caused by water adsorption. At this point, the main conclusion is that our proposed class of model particles can, indeed, be tuned to describe both gradual and rapid transitions in LDR as a result of water coating.

Size-averaged results are rather sensitive to which size distribution we assume. We use a generic lognormal size distribution, which allowed us to cover a range of effective radii from 0.15 to 1.1μm. One obtains a correspondingly wide range of size-averaged optical properties. When restricting the range of median dry radii to about $0.4\,\mu\text{m} \leq r_{\text{med}}^{\text{dry}} \leq 0.8\,\mu\text{m}$, then the range of computed lidar ratios and the LDRs is consistent with existing field and satellite observations. The modified power-law size [8], which had been derived from earlier work of size distribution measurements of marine particles [47,48], gives size-averaged optical properties that are fully consistent with field data for the entire range of the slope parameter α.

Homogeneous cubic superellipsoids with a roundness parameter of 0.6 in conjunction with the power-law size distribution give results for $\bar{C}_{\text{ext}}$, $\bar{C}_{\text{bak}}$, and the lidar ratio that agree with the reference model. For f_m=0.97, the ensemble-averaged LDR of superellipsoids is slightly lower than that obtained by the reference model, while for f_m=0.91, the reference model gives lower results. However, by allowing the superellipsoids to become elongated the LDR can be tuned. For f_m=0.97, a rather mild elongation of $c/a = 1.25$ already had a significant effect, which roughly doubled the LDR compared to cubic superellipsoids with $b/a = c/a = 1$.

By introducing our model in this manuscript and demonstrating its suitability for modelling size-averaged optical properties of dissolving sea salt aerosol, we laid the ground work for further studies extending the applicability of our model to additional wave-

lengths. In fact, we expect an increasing availability of simultaneous lidar ratio and depolarization ratio measurements at 1064 nm, following the work in [58] on rotational Raman measurements, and the observational studies in, e.g., [59–61]. We believe that evaluating the model simultaneously at additional wavelengths could improve the robustness of the model, and it might help to further refine the model by constraining its free parameters, warranting further studies despite the high computational demand. Sufficiently constrained, our model will become a helpful, if computationally expensive tool to relate optical and microphysical properties, and thus improve the interpretation of lidar measurements.

Apart from laboratory studies, field and satellite measurements of lidar depolarisation ratios in conjunction with meteorological data may be helpful to better tune both our reference model and simplified models, such as homogeneous or inhomogeneous superellipsoids. Examples of such measurements have been reported in [24,54,55]. The main challenge is to select observations of marine aerosols that are not influenced by particles other than sea salt, since long-range transported marine aerosols can often be mixed with sulphate, nitrate, mineral dust, and other aerosols [62]. Another prerequisite is to accurately retrieve the size distribution of the aerosols prior to tuning the model morphology of the water-coated particles.

In summary, the reference model is tunable to cover a large range of optical properties, and to mimic both slow and fast transitions from high to vanishing LDR as a result of water adsorption. The size-averaged optical properties depend not only on the effective radius, but also on the form of the size distribution. In our study, we leaned toward the parameterisation in [8]; it models the size-resolved flux of particles from water to air based on not only wind speed, but also sea-surface temperature and salinity. The latter two have a significant impact on the size distribution, but they are often neglected in other studies [46]. More guidance on how to tune our model will depend on better constraining the size distribution of marine particles by observations. Presently, we have a number of different models for the size distribution of marine particles, comprising mono-modal [13] and bi-modal [46] lognormal distributions, as well as various power-law distributions [8,47,48]. These models are derived from size distribution measurements. For instance, the measurements by [48] cover a large part of the size spectrum (radii 0.01–10.0μm) with high size resolution (41 bins). The observed particles were generated by bubble bursting, thus mimicking one of the main production mechanisms of marine aerosols in nature. But these measurements were not accompanied by any observations of the aerosols' optical properties. On the other hand, we have simultaneous measurements by [13] of the size distribution and of optical properties of marine aerosols. But these size-distribution measurements only covered a limited part of the size spectrum (radii 0.15–2.5μm) with a limited size resolution (five bins). Also, the salt aerosols were produced by a nebulizer. It is not entirely clear to what extent this method produces realistic proxies of natural marine particles. In fact, a recent comparison revealed that a nebulizer produces size distributions of aerosols that are substantially different from those produced by bubble bursting [63]. Further modelling progress will depend on experimental studies that (i) consider salt aerosols representative of marine aerosols in nature; (ii) cover a large part of the size spectrum from the Aitken mode to the coarse mode; and (iii) provide simultaneous measurements of aerosol optical properties, especially the backscattering cross section and LDR. It would also be desirable to study proxies of marine aerosols generated for different water temperatures and for a range of salinities. Such comprehensive investigations could help us to better constrain the size distribution, and to tune the morphology of our reference model to best describe the transition from depolarising nonspherical particles to non-depolarising spherical droplets.

Credit Author Statment

M. Kahnert contributed with conceptualization, model development and runs, data analysis, and writing, as well as funding acquisistion and project administration.

F. Kanngießer contributed with conceptualization, model development and runs, data analysis, and writing.

Declaration of Competing Interest

The authors declare the following financial interests/personal relationships which may be considered as potential competing interests:

First author serves as handling editor for JQSRT - MK

Acknowledgements

This project was funded by the Swedish National Space Agency *Rymdstyrelsen* under contract 100/16.

Appendix A. Wet radius and volume fraction of water-coated marine particles with prescribed mass fraction

The process of water condensation onto salt particles gives rise to a brine coating that has a density different from that of water. As a result, the relation between the volume of the composite particles to that of its separate constituents is not as trivial as it is for particles composed of insoluble components, such as sulphate-coated black carbon aerosols. Optical properties of particles strongly depend on their size, which is related to the particle volume. For this reason, one often characterises optical properties of composite particles in terms of the volume fraction of their constituents. However, one motivation for developing aerosol-optics models is to assist in the evaluation of chemical transport models (CTMs), which are *mass*-transport models. Therefore, it is desirable to express optical properties of composite particles in terms of the mass fraction of their constituents. Here we briefly discuss how the salt mass fraction is related to the volume fraction and the wet radius.

Let us denote the mass density of dry salt and of saturated salt solution by ρ_s and ρ_b, respectively (where the subscript b stands for brine). We further denote the mass fraction of a saturated sea-salt solution by

$$\phi_b = \frac{m_s^{\text{solute}}}{m_w} \tag{A.1}$$

where m_s^{solute} is the salt-mass in a saturated solution, and m_w is the mass of water. At a temperature of 283 K ϕ_b=0.36 kg salt/kg water [64]. We further use ρ_s=2240 kg/m^3 and ρ_b=1210 kg/m^3 [18]. The mass fraction of a water-coated salt particle is given by

$$f_m = \frac{m_s^{\text{tot}}}{m_w + m_s^{\text{tot}}}, \tag{A.2}$$

where m_s^{tot} is the total salt mass in the composite particle, i.e., comprising both the mass of salt in solution and that remaining in the solid salt core. The mass of the salt core is given by $m_s^{\text{core}} = m_s^{\text{tot}} - m_s^{\text{solute}} = m_s^{\text{tot}} - m_w\phi_b$, hence

$$m_s^{\text{core}} = \left[1 - \frac{1-f_m}{f_m}\phi_b\right] m_s^{\text{tot}}. \tag{A.3}$$

Thus the mass $m_s^{\text{solute}} = m_s^{\text{tot}} - m_s^{\text{core}}$ is given by

$$m_s^{\text{solute}} = \frac{1-f_m}{f_m}\phi_b m_s^{\text{tot}}. \tag{A.4}$$

The mass of the liquid mantle is given by $m_b = m_w + m_s^{\text{solute}} = V_b\rho_b$, where V_b is the volume of the mantle. Using Eq. (A.4) as well as $m_w = m_s^{\text{tot}}(1-f_m)/f_m$, this yields

$$V_b = \frac{1}{\rho_b}\cdot\frac{1-f_m}{f_m}(1+\phi_b)\,m_s^{\text{tot}}. \tag{A.5}$$

The volume of the core is given by $V_s^{\text{core}} = m_s^{\text{core}}/\rho_s$. Using Eqs. (A.3) and (A.5), we obtain the total particle volume

$$V^{\text{tot}} = \left\{\frac{1-f_m}{f_m}\left[\frac{1+\phi_b}{\rho_b} - \frac{\phi_b}{\rho_s}\right] + \frac{1}{\rho_s}\right\} m_s^{\text{tot}}. \tag{A.6}$$

From this we obtain the wet radius, i.e., the volume-equivalent radius of the composite particle r_{wet}

$$r_{\text{wet}} = \left\{\frac{3}{4\pi}m_s^{\text{tot}}\left[\frac{1-f_m}{f_m}\left(\frac{1+\phi_b}{\rho_b} - \frac{\phi_b}{\rho_s}\right) + \frac{1}{\rho_s}\right]\right\}^{1/3}. \tag{A.7}$$

The dry radius of the salt particle prior to adding water is given by $r_{\text{dry}} = [3m_s^{\text{tot}}/(4\pi\,\rho_s)]^{1/3}$, so that

$$r_{\text{wet}} = r_{\text{dry}}\left\{\frac{1-f_m}{f_m}\left[(1+\phi_b)\frac{\rho_s}{\rho_b} - \phi_b\right] + 1\right\}^{1/3}. \tag{A.8}$$

With this we can convert the mass fraction into the volume fraction $f_v = r_{\text{dry}}^3/r_{\text{wet}}^3$, which gives

$$f_v = \left\{\frac{1-f_m}{f_m}\left[(1+\phi_b)\frac{\rho_s}{\rho_b} - \phi_b\right] + 1\right\}^{-1}. \tag{A.9}$$

References

[1] Fan J, Wang Y, Rosenfeld D, Liu X. Review of aerosol-cloud interactions: Mechanisms, significance, and challenges. J Atmos Sci 2016;73:4221–52.
[2] Meijers AJS. The southern ocean in the coupled model intercomparison project phase 5. Phil Trans R Soc A 2014;372:20130296.
[3] Bodas-Salcedo A, Williams KD, Ringer MA, Beau I, Cole JNS, Dufresne J-L, Koshiro T, Stevens B, Wang Z, Yokohata T. Origins of the solar radiation biases over the southern ocean in CFMIP2 models. J Climate 2014;27:41–56.
[4] Soares J, Sofiev M, Geels C, Christensen JH, Andersson C, Tsyro S, et al. Impact of climate change on the production and transport of sea salt aerosol on European seas. Atmospheric Chemistry and Physics 2016;16(20):13081–104. doi:10.5194/acp-16-13081-2016.
[5] Kahnert M. Modelling the optical and radiative properties of freshly emitted light absorbing carbon within an atmospheric chemical transport model. Atmos Chem Phys 2010;10:1403–16.
[6] Andersson E, Kahnert M. Coupling aerosol optics to the MATCH (v5. 5.0) chemical transport model and the SALSA (v1) aerosol microphysics module. Geosci Model Dev 2016;9:1803–26.
[7] Lewis ER, Schwartz SE. Sea salt aerosol production: mechanisms, methods, measurements and models: a critical review. Washington, DC: Americal Geophysical Union; 2004.
[8] Sofiev M, Soares J, Prank M, de Leeuw G, Kukkonen J. A regional-to-global model of emission and transport of sea salt particles in the atmosphere. J Geophys Res 2011;116:D21302.
[9] Chamaillard K, Jennings SG, Kleefeld C, Ceburnis D, Yoon YJ. Light backscattering and scattering by nonspherical sea-salt aerosols. J Quant Spectrosc Radiat Transfer 2003;79–80:577–97.
[10] Gwaze P, Helas G, Annegarn HJ, Huth J, Piketh SJ. Physical, chemical and optical properties of aerosol particles collected over Cape Town during winter haze episodes. S Afr J Sci 2007;103:35–43.
[11] Murayama TH, Okamoto H, Kaneyasu N, Kamataki H, Miura K. Application of lidar depolarization measurement in the atmospheric boundary layer: Effects of dust and sea-salt particles. J Geophys Res 1999;104(D24):31781–92. doi:10.1029/1999JD900503.
[12] Chamaillard K, Kleefeld C, Jennings S, Ceburnis D, O'Dowd C. Light scattering properties of sea-salt aerosol particles inferred from modeling studies and ground-based measurements. J Quant Spectrosc Radiat Transfer 2006;101(3):498–511. doi:10.1016/j.jqsrt.2006.02.062. Light in Planetary Atmospheres and Other Particulate Media
[13] Sakai T, Nagai T, Zaizen Y, Mano Y. Backscattering linear depolarization ratio measurements of mineral, sea-salt, and ammonium sulfate particles simulated in a laboratory chamber. Appl Opt 2010;49(23):4441–9. doi:10.1364/AO.49.004441.
[14] David G, Thomas B, Nousiainen T, Miffre A, Rairoux P. Retrieving simulated volcanic, desert dust and sea-salt particle properties from two/three-component particle mixtures using UV-VIS polarization lidar and T matrix. Atmos Chem Phys 2013;13:6757–76. doi:10.5194/acp-13-6757-2013.
[15] Adachi K, Buseck PR. Changes in shape and composition of sea-salt particles upon aging in an urban atmosphere. Atmos Environ 2015;100:1–9. doi:10.1016/j.atmosenv.2014.10.036.
[16] Bi L, Lin W, Liu D, Zhang K. Assessing the depolarization capabilities of nonspherical particles in super-ellipsoidal shape space. Opt Express 2018;26:1726–42.
[17] Bi L, Lin W, Wang Z, Tang X, Zhang X, Yi B. Optical modeling of sea salt aerosols: The effects of nonsphericity and inhomogeneity. J Geophys Res 2018;123:543–58.
[18] Kanngießer F, Kahnert M. Optical properties of water-coated sea salt model particles. Opt Express 2021;29:34926–50.
[19] Kanngießer F, Kahnert M. Modeling optical properties of non-cubical sea-salt particles. J Geophys Res: Atmospheres 2021;126. e2020JD033674
[20] Kahnert FM, Stamnes JJ, Stamnes K. Application of the extended boundary condition method to particles with sharp edges: A comparison of two different surface integration approaches. Appl Opt 2001;40:3101–9.
[21] Kahnert FM, Stamnes JJ, Stamnes K. Application of the extended boundary condition method to homogeneous particles with point group symmetries. Appl Opt 2001;40:3110–23.
[22] Kahnert M. On the observability of chemical and physical aerosol properties by optical observations: Inverse modelling with variational data assimilation. Tellus 2009;61B:747–55.
[23] Kahnert M. Information constraints in variational data assimilation. Q J R Meteorol Soc 2018;144:2230–44.
[24] Haarig M, Ansmann A, Gasteiger J, Kandler K, Althausen D, Baars H, Radenz M, Farrell DA. Dry versus wet marine particle optical properties: RH dependence of depolarization ratio, backscatter, and extinction from multiwavelength lidar measurements during SALTRACE. Atmos Chem Phys 2017;17(23):14199–217. doi:10.5194/acp-17-14199-2017.
[25] King SM, Butcher AC, Rosenoern T, Coz E, Lieke KI, de Leeuw G, Nilsson ED, Bilde M. Investigating primary marine aerosol properties: CCN activity of sea salt and mixed inorganic-organic particles. Environ Sci Technol 2012;46(19):10405–12. doi:10.1021/es300574u.
[26] McInnes LM, Covert DS, Quinn PK, Germani MS. Measurements of chloride depletion and sulfur enrichment in individual sea-salt particles collected from the remote marine boundary layer. Journal of Geophysical Research: Atmospheres 1994;99(D4):8257–68. doi:10.1029/93JD03453.
[27] Patterson JP, Collins DB, Michaud JM, Axson JL, Sultana CM, Moser T, Dommer AC, Conner J, Grassian VH, Stokes MD, Deane GB, Evans JE, Burkart MD, Prather KA, Gianneschi NC. Sea spray aerosol structure and composition using cryogenic transmission electron microscopy. ACS Cent Sci 2016;2(1):40–7. doi:10.1021/acscentsci.5b00344.
[28] Peart A, Evans JRG. Study of sea salt particles launched by bubble burst. Bub Sci Eng Technol 2011;3(2):64–72. doi:10.1179/1758897911Y.0000000004.
[29] Zeng J, Zhang G, Long S, Liu K, Cao L, Bao L, Li Y. Sea salt deliquescence and crystallization in atmosphere: an in situ investigation using x-ray phase contrast imaging. Surf Interface Anal 2013;45(5):930–6. doi:10.1002/sia.5184.
[30] Wise ME, Biskos G, Martin ST, Russell LM, Buseck PR. Phase transitions of single salt particles studied using a transmission electron microscope with an environmental cell. Aerosol Sci Technol 2005;39(9):849–56. doi:10.1080/02786820500295263.
[31] Torge A, Macke A, Heinold B, Wauer J. Solar radiative transfer simulations in Saharan dust plumes: particle shapes and 3-D effect. Tellus B 2011;63(4):770–80. doi:10.1111/j.1600-0889.2011.00560.x.
[32] Ishimoto H, Kudo R, Adachi K. A shape model of internally mixed soot particles derived from artificial surface tension. Atmos Meas Tech 2019;12:107–18.
[33] Eldridge J, Palik ED. Sodium chloride (NaCl). In: Palik ED, editor. Handbook of Optical Constants of Solids. Burlington: Academic Press; 1997. p. 775–93. ISBN 978-0-12-544415-6. doi:10.1016/B978-012544415-6.50041-8.
[34] Li X, Liu L, Zhao J, Tan J. Optical properties of sodium chloride solution within the spectral range from 300 to 2500 nm at room temperature. Appl Spectrosc 2015;69(5):635–40. http://as.osa.org/abstract.cfm?URI=as-69-5-635
[35] Wriedt T. Using the T-matrix method for light scattering computations by non-axisymmetric particles: Superellipsoids and realistically shaped particles. Part Part Sys Charact 2002;19(4):256–68. doi:10.1002/1521-4117(200208)19:4<256::AID-PPSC256>3.0.CO;2-8.
[36] Maxwell Garnett JC. Colours in metal glasses and in metallic films. Philos Trans R Soc A 1904;203:385–420.
[37] Kahnert M. Numerical solutions of the macroscopic Maxwell equations for scattering by non-spherical particles: A tutorial review. J Quant Spectrosc Radiat Transfer 2016;178:22–37.
[38] Yurkin MA, Hoekstra AG. The discrete-dipole-approximation code ADDA: Capabilities and known limitations. J Quant Spectrosc Radiat Transfer 2011;112:2234–47.
[39] Kahnert M. The T-matrix code Tsym for homogeneous dielectric particles with finite symmetries. J Quant Spectrosc Radiat Transfer 2013;123:62–78.
[40] Waterman PC. Symmetry, unitarity, and geometry in electromagnetic scattering. Phys Rev D 1971;3:825–39.
[41] Schulz FM, Stamnes K, Stamnes JJ. Point group symmetries in electromagnetic scattering. J Opt Soc Am A 1999;16:853–65.
[42] Kahnert M. Irreducible representations of finite groups in the T matrix formulation of the electromagnetic scattering problem. J Opt Soc Am A 2005;22:1187–99.
[43] Mishchenko MI. Light scattering by randomly oriented axially symmetric particles. J Opt Soc Am A 1991;8:871–82.

[44] Khlebtsov NG. Orientational averaging of light-scattering observables in the T–matrix approach. Appl Opt 1992;31:5359–65.
[45] Mishchenko MI, Travis LD, Lacis AA. Scattering, absorption, and emission of light by small particles. Cambridge: Cambridge University Press; 2002.
[46] Porter JN, Clarke AD. Aerosol size distributions models based on in situ measurements. J Geophys Res 1997;102:6035–45.
[47] Monahan EC, Spiel DE, Davidson KL. A model of marine aerosol generation via whitecaps and wave disruption. In: Monahan EC, Niocaill GM, editors. Oceanic Whitecaps and their role in air-sea exchange. Norwell, MA: D Reidel; 1986. p. 167–74.
[48] Mårtensson EM, Nilsson ED, de Leeuw G, Cohen LH, Hansson H-C. Laboratory simulations and parameterization of the primary marine aerosol production. J Geophys Res 2003;108:D9,4297.
[49] Andersson C, Bergström R, Bennet C, Robertson L, Thomas M, Korhonen H, Lehtinen KHJ, Kokkola H. MATCH-SALSA — multi-scale atmospheric transport and CHemistry model coupled to the SALSA aerosol microphysics model — Part 1: Model description and evaluation. Geosci Model Dev 2015;8:171–89.
[50] Simpson D, Benedictow A, Berge H, Bergström R, Emberson LD, Fagerli H, et al. The Emep MSC-W chemical transport model — technical description. Atmos Chem and Phys 2012;12(16):7825–65. doi:10.5194/acp-12-7825-2012.
[51] O'Dowd CD, Smith MH, Consterdine IE, Lowe JA. Marine aerosol, sea salt, and the marine sulphur cycle: A short review. Atmos Environ 1997;31:73–80.
[52] Mishchenko MI, Lacis AA, Carlson BE, Travis LD. Nonsphericity of dust-like tropospheric aerosols: implications for aerosol remote sensing and climate modeling. Geophys Res Lett 1995;22:1077–80.
[53] Tang IN, Tridico AC, Fung KH. Thermodynamic and optical properties of sea salt aerosols. J Geophys Res 1997;102:23269–75.
[54] Ferrare R, Hair J, Hostetler C, Harper D, Seaman S, Shingler T, Crosbie E, Winstead E, Ziemba L, Thornhill K, Fenn M, Clayton M, Scarino A, Burton S, Cook A, Diskin G, Moore R, Robinson C, DiGangi J, Nowak J, Choi Y, Schlosser J, Sorooshian A, van den Heever S. Variability in aerosol properties associated with changes in relative humidity as measured by the airborne high spectral resolution lidar-2. AGU Fall Meeting. New Orleans: AGU; 2021. 2021AGUFM.A13B..02F
[55] Thomas MA, Devasthale A, Kahnert M. Marine aerosol properties over the Southern Ocean in relation to the wintertime meteorological conditions. Atmos Chem Phys 2022;22:119–37. doi:10.5194/acp-22-119-2022.
[56] Kahnert M. Modelling radiometric properties of inhomogeneous mineral dust particles: Applicability and limitations of effective medium theories. J Quant Spectrosc Radiat Transfer 2015;152:16–27.
[57] Nousiainen T, Kahnert M, Lindqvist H. Can particle shape information be retrieved from light-scattering observations using spheroidal model particles? J Quant Spectrosc Radiat Transfer 2011;112:2213–25. doi:10.1016/j.jqsrt.2011.05.008.
[58] Veselovskii I, Whiteman DN, Korenskiy M, Suvorina A, Pérez-Ramírez D. Use of rotational raman measurements in multiwavelength aerosol lidar for evaluation of particle backscattering and extinction. Atmospheric Measurement Techniques 2015;8(10):4111–22. doi:10.5194/amt-8-4111-2015.
[59] Haarig M, Engelmann R, Ansmann A, Veselovskii I, Whiteman DN, Althausen D. 1064 nm rotational raman lidar for particle extinction and lidar-ratio profiling: cirrus case study. Atmos Meas Tech 2016;9(9):4269–78. doi:10.5194/amt-9-4269-2016.
[60] Haarig M, Ansmann A, Baars H, Jimenez C, Veselovskii I, Engelmann R, et al. Depolarization and lidar ratios at 355, 532, and 1064 nm and microphysical properties of aged tropospheric and stratospheric Canadian wildfire smoke. Atmos Chem Phys 2018;18(16):11847–61. doi:10.5194/acp-18-11847-2018.
[61] Haarig M, Ansmann A, Engelmann R, Baars H, Toledano C, Torres B, et al. First triple-wavelength lidar observations of depolarization and extinction-to-backscatter ratios of Saharan dust. Atmospheric Chemistry and Physics 2022;22(1):355–69. doi:10.5194/acp-22-355-2022.
[62] Sakai T, Nagai T, Mano Y, Zaizen Y, Inomata Y. Aerosol optical and microphysical properties as derived from collocated measurements using polarization lidar and direct sampling. Atmos Env 2012;60:419–27.
[63] Ickes L, Porter GCE, Wagner R, Adams MP, Bierbauer S, Bertram AK, Bilde M, Christiansen S, Ekman AML, Gorokhova E, Höhler K, Kiselev AA, Leck C, Möhler O, Murray BJ, Schiebel T, Ullrich R, Salter ME. The ice-nucleating activity of arctic sea surface microlayer samples and marine algal cultures. Atmos Chem and Phys 2020;20(18):11089–117. https://acp.copernicus.org/articles/20/11089/2020/
[64] Lide DR. CRC Handbook of Chemistry and Physics. Boca Raton: CRC Press; 2000.